Response to the comments of Referee #1

Dear Reviewer,

We sincerely thank the reviewers for the thorough and constructive comments, which have substantially improved the manuscript. We have carefully addressed all comments point by point below. In this response letter, our replies to each comment are presented in blue text, and revised manuscript text is highlighted in yellow. All changes are indicated in the revised manuscript using tracked changes.

.....

Referee #1:

Lim et al. present observations of non-refractory aerosol from an aerosol mass spectrometer, black carbon, and limited volatile organic compounds (VOCs) from a proton transfer reaction mass spectrometer from 6 research flights that was conducted across three days over the Yellow Sea. They use the observations to investigate trends and driving factors of black carbon coating thickness. Currently as written, the paper is lacking detailed analysis, appropriate comparisons and discussions within broader literature, and appropriate understanding and description of the chemical and physical drivers impacting the observed trends in the various aerosol component reported here, as discussed below. Due to this, the paper does not appear ready or appropriate for ACP.

1. Though OpenAI is acknowledged for grammar and language editing, either another AI tool or a person should review the article for grammar, flow, and understanding prior to next submission.

We appreciate this suggestion. The entire manuscript has undergone comprehensive

proofreading and editing by a professional scientific language editing service specializing in atmospheric sciences. We have thoroughly revised the text to improve grammatical precision, sentence structure, and overall clarity and flow throughout the revised manuscript.

2. Introduction could use more motivation and clarification about the problem and the uncertainty. As written, it was not even clear that much of the introduction was based on observations in East Asia or Yellow Sea region. Further, how does this problem occur outside just East Asia?

We thank the reviewer for these valuable suggestions to improve the motivation, geographic context, and global relevance in the Introduction. We have substantially revised Introduction to address each point.

1. Introduction

Aerosols significantly impact regional air quality and the global climate system. Black carbon (BC), a primary, light-absorbing aerosol originating from incomplete combustion, plays a critical role in regional air quality and global climate systems (Bond et al., 2013). While fresh BC aerosols are largely hydrophobic and chemically inert, in the atmosphere they undergo complex aging processes, by which BC aerosols are internally mixed with other components. Through coagulation and condensation, they form coating materials and ultimately changing in morphology, size, chemical composition, and light-absorption properties, signifying their air quality and climate impacts (Mishra et al., 2026 and references therein), introducing profound uncertainties into model predictions of BC direct radiative forcing (Cappa et al., 2012; Liu et al., 2017).

In general, while condensation of low volatile and oxygenated gases forms secondary aerosol on BC surfaces, the amount of secondary aerosol coating and its formation rate depend on complex atmospheric chemical and physical state and its interplay with meteorology (Lim et al., 2023, 2025; Peng et al., 2016; Riemer et al., 2010). In East Asia, the mixing state and secondary coating of BC exhibit pronounced seasonality with thicker in winter and thinner coatings in summer (Kompalli et al., 2020; Liu et al., 2019), which is tightly coupled with ambient PM loadings and meteorological conditions. Specifically, observations in urban Seoul demonstrate this sharp contrast. During warm summertime under clean marine influence, the majority of BC particles (>70%) remain bare or thinly coated with daytime coating growth rates of a few nm per hour in daytime largely due to limited condensable materials as well as high air temperature, e.g. above 25 °C (Lim et al., 2023). In contrast, during transboundary winter haze periods, BC aerosols were thickly coated and highly associated with the chemical oxidation state of the atmosphere (Lim et al., 2025). While daytime photochemical activity and nocturnal aqueous-phase chemistry have been recognized as key drivers of secondary nitrate and sulfate formation associated with BC coating in continental urban environments (Zhang et al., 2021; Cui et al., 2022; Zhou et al., 2022; Wei et al., 2023), notable observations indicate that highly internally mixed and thickly coated BC aerosols are ubiquitously observed not only in heavily polluted downwind megacities (e.g., Seoul) but also at regional background sites (e.g., Gosan Climate Observatory in Jeju Island; Lim et al., 2023). Transboundary pollution plumes likely undergo vigorous chemical and physical aging while traversing the Yellow Sea. However, the quantitative relationship linking BC physical coating growth to bulk aerosol chemical evolution and precursor availability during transboundary transport over the marine boundary layer remains poorly understood.

This knowledge gap has fundamental implications that extend well beyond East Asia. In

remote polar regions such as the Arctic, BC aerosols transported over thousands of kilometers frequently exhibit strong internal mixing state and high absorption enhancement (Zanatta et al., 2018; Teng et al., 2026), yet the specific physical and chemical transformations occurring along long-range transport pathways remain a major unresolved question in global climate science.

The Yellow Sea, situated between the massive emission sources of the Asian countries and downwind receptor regions, servers as a critical place for observing the real-time physical aging and chemical evolution of continental outflows over an open marine boundary layer (e.g., Takegawa et al., 2020). Although Yu et al. (2025) recently documented multi-seasonal BC physical properties in relation to combustion indicators over the Yellow Sea, the detailed chemical drivers governing size-resolved coating evolution during acute haze episodes remain unconstrained. In particular, as emission sources and intensity are rapidly changing in East Asia (Kanaya et al., 2020), establishing comprehensive multi-pollutant mitigation strategies requires a precise understanding of how these evolving chemical environments dictate secondary aerosol coatings and BC physical aging.

In this study, we present a recent airborne measurement over the Yellow Sea during a wintertime 3-day haze episode that occurred in December 2025. We investigate interplay of bulk chemical composition of fine aerosol and BC physical aging, focusing on temporal evolution from the pre-episode period through the stagnant aging phase to the haze clearance.

3. The methods need substantially more information. What is the diameter and residence time for the aerosol measurements? Was ram heating used for a drier? How was cloud sampling treated? Was inlet forward or backward facing? Was same inlet used for PTR as the aerosol

instruments? How were the different instruments time-aligned? What "bounce" was used for AMS data? What lens was used for AMS (PM1 or PM2.5)? What was the particle transmission through all the lines? Were cals conducted before or after each flight, each day, only at beginning and end of campaign? Why are charges included in the description of nitrate, sulfate, and ammonium? As both inorganic and organic species can lead to the ions observed for these three aerosol species, charged symbols should not be included as there is inherent uncertainty how much organic nitrate, organic sulfate, and organic reduced nitrogen species maybe contributing to the whole.

We agree that the methods need substantially more information. In the revised manuscript, this information has been added to the revised Methods section such as below sentences.

1) What is the diameter and residence time for the aerosol measurements? Was ram heating used for a drier? How was cloud sampling treated? Was inlet forward or backward facing? Was same inlet used for PTR as the aerosol instruments? How were the different instruments time-aligned?

L112-135:

All instruments were synchronized before each flight to the onboard GPS-referenced time server through the aircraft Ethernet network. AIMMS-30 independently acquired GPS-referenced position and time information.

Aerosol and gas-phase sampling lines were physically separated to prevent cross-contamination and sampling artifacts. For aerosol sampling, ambient air was drawn through a commercial isokinetic Airborne Aerosol Inlet (Droplet Measurement Technologies, USA) with oriented forward in roof. The primary inlet flow rate was strictly maintained at 100 L min^{-1}

to ensure isokinetic sampling and minimize flow-distortion-induced particle losses during flight. The inlet used for the present measurements was connected to the High-Resolution Time-of-Flight Aerosol Mass Spectrometer (HR-ToF-AMS, Aerodyne Research Inc., USA) and the Single Particle Soot Photometer (SP2, Droplet Measurement Technologies, USA) through stainless tubing with an inner diameter of 0.25 inch and a total length of 1.2 m. Based on the corresponding flow rates, the estimated transport times from the aircraft inlet to the HR-ToF-AMS and SP2 were 0.8 s and 0.4 s, respectively. The Airborne Aerosol Inlet (AAI) was equipped with an anti-icing heater designed for operation under extremely cold and humid conditions. The inlet heater and an aerosol dryer were not used during the flights analyzed in this study because such icing conditions were not encountered and most measurements were conducted at approximately 300 m altitude. Thus, aerosol samples were introduced to instruments without heating or drying. For gas measurements, gas-phase samples were collected through a dedicated forward-facing Trace Gas Inlet (TGI) designed by the University of California, Irvine (UCI) and flight-proven during the KORUS-AQ campaign (Jeong et al., 2019). Two independent TGIs were mounted on the forward left and right sides of the aircraft fuselage, and the PTR-ToF-MS sampled continuously through the starboard (right-side) inlet via a heated PFA Teflon line. Cloud sampling was not performed during the flights analyzed here, as all flight paths strictly avoided cloud encounters based on flight logs and in situ meteorological observations.

2) What "bounce" was used for AMS data? What lens was used for AMS (PM1 or PM2.5)? What was the particle transmission through all the lines? Were cals conducted before or after each flight, each day, only at beginning and end of campaign?

L178-206:

The mass concentrations and chemical compositions of non-refractory submicron particulate

matter with and aerodynamic diameter of less than 1 μm ($NR\text{-}PM_1$), including organics, sulfate, nitrate, and ammonium, were characterized in real-time utilizing a High-Resolution Time-of-Flight Aerosol Mass Spectrometer (HR-ToF-AMS, Aerodyne Research Inc., USA) (DeCarlo et al., 2006). When the ambient air entered the HR-ToF-AMS inlet, aerosols were passed to a pressure-controlled inlet (PCI) that was installed upstream inlet for making a constant flow rate of 1.3 LPM independent of altitude changes (Ban et al., 2024). Inside the instrument, sampled aerosols were passed through the critical orifice and the standard PM_1 aerodynamic lens to make a narrow beam of particles under a vacuum environment in the chamber from installed turbo pumps (Ban et al., 2024; Park et al., 2020). A chopper positioned inside the chamber alternates between open and closed states, thereby controlling the particle beam's access to the vaporizer (Canagaratna et al., 2007). The passed aerosols directed onto a heated standard vaporizer operating at 600 °C, where the non-refractory components were flash-vaporized and subsequently ionized via 70 eV electron impact (Alfarra et al., 2004; Jayne et al., 2000). Within the ToF chamber, the generated ions are segregated by their mass-to-charge (m/z) ratios based on flight-time differences, enabling both species identification and subsequent concentration quantification from the measured signal intensities (Park et al., 2025).

To ensure sufficient temporal resolution for capturing rapid atmospheric variations during the flights, the HR-ToF-AMS was operated exclusively in Fast-MS (FMS) mode (Kimmel et al., 2011). Mass spectral data processing and quantification were carried out utilizing the Igor Pro-based software packages, SQUIRREL (v1.67) and PIKA (v1.27) (DeCarlo et al., 2006). Calibrations for the instrumental sensitivity, ionization efficiency (IE) and relative ionization efficiencies (RIEs) were performed three times during the campaign: at the beginning, midpoint, and end of the measurement period using ammonium nitrate (NH_4NO_3), ammonium sulfate ($(NH_4)_2SO_4$), and ammonium chloride (NH_4Cl) particles produced by an aerosol

portable atomizer (TSI Incorporated, USA) (Canagaratna et al., 2007). The determined IE and RIE values were subsequently applied to the dataset to quantify aerosol mass concentrations. Particle bounce at the standard vaporizer was corrected using a composition-dependent collection efficiency (CDCE) following Middlebrook et al. (2012), with a nominal CE of 0.5. The applied CE was allowed to vary according to aerosol composition rather than using a constant CE throughout the campaign.

3) Why are charges included in the description of nitrate, sulfate, and ammonium? As both inorganic and organic species can lead to the ions observed for these three aerosol species, charged symbols should not be included as there is inherent uncertainty how much organic nitrate, organic sulfate, and organic reduced nitrogen species maybe contributing to the whole.

We agree that the use of charged symbols (NO_3^-, SO_4^{2-}, and NH_4^+) may imply that the AMS measurements only represent inorganic ionic species. In the HR-ToF-AMS, mass concentrations of nitrate, sulfate, and ammonium are derived from their fragment ions by electron impaction. These signals may include contributions from organo-nitrate, organo-sulfate, and other compounds species. Therefore, the molecular forms contributing to the HR-ToF-AMS can't be exactly determined from the bulk mass spectra used in this study. Accordingly, we have replaced NO_3^-, SO_4^{2-}, and NH_4^+ with "nitrate", "sulfate", and "ammonium" in the manuscript, figures, and tables.

4. The authors state many values and that they are different. However, looking at the values, it is hard to discern if they are statistically different or not. The error bars in Fig. 2, 4, and 5 generally makes it appear that there is minimal statistical difference in

coating thickness, make it difficult to determine if the changes observed during the flights are real.

We have thoroughly reviewed the manuscript to ensure that comparisons between measured values across different flight stages, altitudes, and chemical regimes are supported by rigorous statistical metrics.

1) Clarification of temporal resolutions across datasets, tables, and figures

First, these numerical discrepancies arise because certain tables report values constrained strictly within the boundary layer, whereas several figures encompass data across all flight altitudes. We clearly indicate time resolution of data used in text, tables, and figures.

L229-235: All datasets obtained from the onboard instruments were synchronized to the time stamp of AIMMS-30. Data of meteorology, NR-PM_1, and VOCs were initially processed at a 1 s time resolution and subsequently averaged to 1 min intervals for statistical summaries presented in the tables. The rBC mass concentration and physical properties were calculated at the same 1 s resolution and integrated with the aerosol chemical composition, VOCs, meteorological, and flight-position datasets. Different temporal resolutions (e.g., 1-s, 10-s, and 1-min averages) are employed across the figures, with the specific resolution applied to each dataset explicitly specified in the corresponding figure captions.

Table 1. Summary of meteorology, gases, and aerosol components observed during each airborne measurement of 15 to 17 Dec. 2025 within the boundary layer over the Yellow Sea. Values are 5^{th} percentile-95^{th} percentile values (mean ± standard deviation) of 1-

min measurements. For the determination of the boundary layer height used in this study, see Supplementary Information S2.

Table 2. Summary of NR-PM and VOCs within the boundary layer for each research flight. Values for NR-PM_1 and its species are mean ± standard deviation (with mass fraction), and VOCs are 5^{th} percentile–95^{th} percentile values (mean ± standard deviation) of 1-min measurements.

Figure 1. Time series of meteorological parameters, trace gases, and aerosol properties observed during all research flights over the Yellow Sea. The continuous timeline concatenates 1-min data from all airborne measurements: (a) flight altitude with the boundary layer (dotted horizontal line); (b) ambient temperature (°C) and relative humidity (RH); (c) wind direction (WD) and wind speed (WS); (d) mass concentration of refractory black carbon (M_{rBC}) and mass median diameter (MMD); (e) coating thickness fraction (F_{thick}); (f) CO and CO_2; (g) O_3 and NO_2; (h) chemical compositions of non-refractory submicron particulate matter (NR-PM_1); and (i) mass fractions and total mass concentration of NR-PM_1.

Figure 2. Research flight-wise vertical profiles of rBC properties (M_{rBC} and F_{thick}) and NR-PM_1 species concentrations observed during the intensive measurement periods: (a) Dec. 15 AM; (b) Dec. 15 PM; (c) Dec. 16 AM; (d) Dec. 16 PM; (e) Dec. 17 AM; and (f) Dec. 17 PM. The data points and error bars represent the mean and standard deviation of 1-s (1-m for F_{thick}) measurements aggregated into 100-m altitude bins. Wider F_{thick} error bars above ~1,600 m (panels a, b) result from reduced rBC number counts aloft. Statistical significance of the vertical gradients across altitude bins was evaluated using Kruskal–Wallis *H* tests for each flight session (Table S1).

Figure 3. Time series of VOC ratios and photochemical age during the intensive measurement

periods. Panel (a) shows the time series of the BZ/TOL and MOH/ACT ratios, and panel (b) illustrates the time series of the non-refractory particulate matter ($NR\text{-}PM_1$), coating thickness fraction (F_{thick}). Data points represent 1-min averages within the boundary layer.

Figure 4. Size-resolved coating sensitivity of rBC to $NR\text{-}PM_1$ major component, (a) Organic, (b) nitrate, (c) sulfate, and (d) ammonium. Bin 1 (100-140 nm), Bin 2 (140-155 nm), and Bin 3 (156-465 nm) indicate size-dependent rBC group. The blue solid line represents the F_{thick} under the lower 25^{th} percentile mass concentrations of each corresponding aerosol species, while the red solid line denotes the F_{thick} under the upper 25^{th} percentile mass concentrations. The bar graph indicates the difference F_{thick} between the upper and lower 25^{th} percentile F_{thick} values. The analysis was conducted using 1-s data. Missing data indicate unavailable AMS measurements. Statistical significance was evaluated using Kruskal–Wallis *H* tests for each $NR\text{-}PM_1$ component (Sect. 3 in the Supplement).

Figure 5. Size-resolved coating sensitivity of rBC to various VOC groups: (a) total VOCs (TVOCs), (b) aromatic VOC, (c) biogenic VOCs (BVOCs), and (d) Oxygenated VOCs (OVOCs). For TVOCs only (a), the baseline F_{thick} for the lower condition was fixed using the values obtained under the lower 25th percentile concentration on the morning of 15 December. The blue solid line represents the coating thickness fraction F_{thick} under the lower 25th percentile concentrations of each corresponding VOC group, while the red solid line denotes the F_{thick} under the upper 25^{th} percentile concentrations. The bar graph indicates the difference (ΔF_{thick}) between the upper and lower 25^{th} percentile F_{thick} values. The analysis was conducted using 1-s data. Statistical significance was evaluated using Kruskal–Wallis *H* tests for each VOC group (Sect. 3 in the Supplement).

2) Interpretive robustness of F_{thick} variations

We acknowledge that the flight-to-flight differences in mean F_{thick} are individually small (within ~10% across the full event), yet the progressive increase in mean F_{thick} from RF1 (0.62) through RF5 (0.70) coincides consistently with a parallel rise in the BZ/TOL ratio (Table 1 and Figure 3), suggesting a physically coherent temporal trend in rBC aging rather than random variability.

In detail, we would like to clarify that the standard deviation (SD) shown in these figures represents the intrinsic particle-to-particle heterogeneity of single-particle rBC mixing states within each bin, rather than the measurement uncertainty or standard error of the mean. Please find the figure below, which is adapted from a recent publication from our research group (Mishra et al., 2026).

As comprehensively compiled across diverse Asian environments in this work, ambient F_{thick} exhibits a characteristic dynamic baseline dictated by site classification and aging state. In the figure abovementioned, some urban sites (e.g., Seoul, Xianyang, Xiamen) include lower F_{thick} baselines (~20-40%), whereas regional background sites (e.g., Noto Peninsula, Lijiang) consistently maintain higher baselines around ~70-80%.

Crucially, within a specific region, the baseline variability (indicated by standard deviations or error bars) is characteristically constrained. Individual regional background sites exhibit narrow variability (error bars within ~5%), such as Noto Peninsula and Lijiang. In contrast, the Yellow Sea airborne dataset exhibits a noticeably larger standard deviation, ~20 %. This broader variability stems directly from the various flight altitude ranges and the multi-year observation span encompassing diverse seasonal transitions, contrasting synoptic regimes, and varying degrees of plume aging across multiple transboundary episodes.

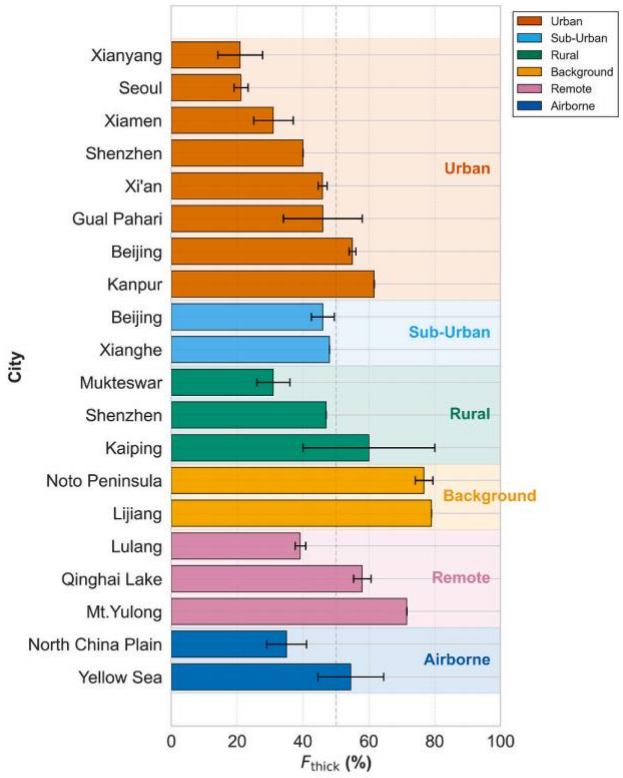

Fig. 7. F_{thick} (Number fraction of Thickly coated particles) of BC in different site types. The values shown are the average and standard deviation (shown with error bars) of all the reported values in a region that has been identified under a specific site category.

Figure R1. F_{thick} of BC in different site types (source: Mishra et al., 2026).

In another study investigating F_{thick} in an urban atmosphere during a single winter period (a month), F_{thick} increased tightly with $PM_{2.5}$, with its mean ~50% to 63% in $PM_{2.5}$ each bin (Lim et al., 2025).

These observational data of F_{thick} demonstrates that within a single targeted winter haze episode, baseline variability remains tightly constrained. Consequently, in Figure 4 and 5, an absolute shift within 20% in F_{thick} reflects a physically meaningful transition in the rBC mixing state rather than instrumental noise.

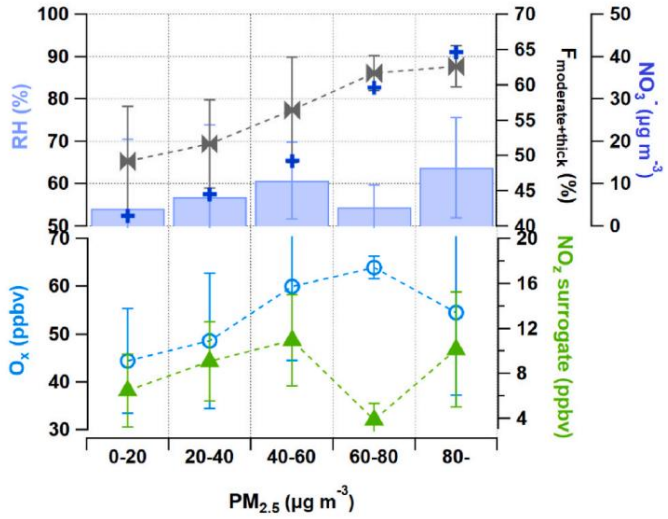

Figure R2. Variations of Fmoderate+thick and other measurement parameters as a function of PM2.5 at urban Seoul in October to November of the 2021. Adapted from Lim et al. (2025).

We added this statement, incorporating the references, Mishra et al. (2026) and Lim et al. (2025) in Section 2.2.

L171-177: It is noteworthy that the variability of F_{thick} (e.g., standard deviation) was often within ~10% at single observation sites in both urban and well-aged background environments (Lim et al., 2025; Shalini et al., 2026). Within a given region and season, baseline fluctuations are tightly bounded. Thus, an absolute shift of ~10% or less is not statistically trivial, but marks a meaningful transition in the BC mixing state.

3) Statistical Significance Test

Regarding figure 2, to directly address whether the vertical variability of F_{thick} across 100-m altitude bins reflects genuine physical gradients rather than observational noise, we

performed non-parametric Kruskal–Wallis H tests across the vertical bins for each individual flight session.

As summarized in the test results below, the vertical gradients of F_{thick} are statistically significant across most flight periods. The weaker statistical significance on 16 Dec. AM ($p < 0.05$) and the lack of significance on 16 Dec. PM are attributable to distinct meteorological and aerosol dispersion conditions. Under relatively stagnant atmospheric condition, NR-PM_1 concentrations were elevated up to 1.8 km a.s.l. on 16 Dec. AM, while high aerosol loadings remained trapped within the boundary layer during the afternoon, resulting in F_{thick} being uniformly distributed. Thus, the absence of sharp vertical differences on 16 Dec. accurately captures a well-mixed, persistent haze layer rather than instrumental insensitivity. In addition, the comparatively moderate statistical significance on 17 Dec. PM ($p<0.05$*) is physically and observationally consistent with the vertical profile (Figure 2f). Within the lower boundary layer (below ~900 m a.s.l.), all aerosol constituents and F_{thick} were vertically well-mixed and uniform, while sparse particle counts in the clean air aloft substantially broadened the F_{thick} uncertainty, inflating the overall p value rather than reflecting measurement ambiguity.*

We have added these Kruskal–Wallis test results to the Supplement (Table S1).

Table S1. Kruskal–Wallis test of vertical F_{thick} variability across 100-m altitude bins for each flight session.

Flight	Total Samples (N)	P value
Dec. 15 AM	157	<0.0001***
Dec. 15 PM	152	<0.0001***
Dec. 16 AM	161	<0.05*
Dec. 16 PM	112	Not significant
Dec. 17 AM	131	<0.01**

Dec. 17 PM	121	<0.05*

Regarding figure 4 and 5, to verify whether the observed differences in F_{thick} between low and high concentration regimes (25th vs. 75th percentiles) were statistically significant, we performed Kruskal–Wallis H tests across each rBC core size bin for individual chemical components and VOC groups.

*The variations in $\triangle F_{thick}$ across individual flight sessions are statistically significant ($p < 0.001$**) across virtually all rBC core size bins for NR-PM_1 components and VOC groups. In the most dominant size range (Bin 2: 140–155 nm, accounting for >8,000 samples), all comparisons yielded the highest significance ($p < 0.0001$***). sulfate alone showed lower statistical robustness ($p > 0.05$). These statistical results confirm that the observed coating thickness responses $\triangle F_{thick}$ depicted in Figure 4 and 5 represent physically driven microphysical transitions. We have incorporated these test results into Sect. S3 in the Supplement and updated the captions of Figures 4 and 5 accordingly.*

5. Much of the meteorological and physicochemical discussions about the aerosols are not cited and incomplete for what may be occurring. Examples include:

a) Consider winds at 4 m/s (9 mph) to be stagnant.

We thank the reviewer for highlighting this meteorological distinction. We agree that a wind speed of approximately 4 m/s does not always constitute absolute synoptic calm. In our analysis, this condition was classified as "stagnant" in relative terms when compared directly to the prevailing synoptic wind fields observed across the flight campaign. Specifically, during the December 16 flights, the mean horizontal wind speeds were 4.07 m/s (morning) and 3.52

m/s (afternoon), which were substantially lower than the wind speeds encountered on the other days (up to 16.0 m/s under strong northerly advection) (Table 1 in the manuscript).

Table 1. Summary of meteorology, gases, and aerosol components observed during each airborne measurement of 15 to 17 Dec. 2025 within the boundary layer over the Yellow Sea. Values are 5th percentile-95th percentile values (mean ± standard deviation) of 1-min measurements.

	Dec. 15 AM	Dec. 15 PM	Dec. 16 AM	Dec. 16 PM	Dec. 17 AM	Dec. 17 PM
Temp. (°C)	-2.29–5.35 (3.89 ± 2.19)	0.58–7.48 (5.62 ± 2.04)	-1.43–9.44 (7.08 ± 3.34)	4.35–10.00 (8.13 ± 1.58)	-1.44–4.78 (3.34 ± 1.78)	-1.47–4.69 (3.08 ± 2.02)
RH (%)	22.6–62.8 (54.1 ± 10.9)	58.9–80.0 (64.8 ± 9.8)	53.1–78.9 (71.6 ± 9.7)	52.1–81.0 (74.2 ± 8.1)	38.8–74.5 (65.5 ± 10.4)	33.2–69.5 (61.3 ± 11.2)
WS ($m\ s^{-1}$)	2.78–10.89 (5.50 ± 2.33)	3.45–9.79 (6.64 ± 2.25)	1.46–8.81 (4.07 ± 2.50)	1.16–8.80 (3.52 ± 2.21)	4.2–24.3 (16.0 ± 6.6)	8.3–12.8 (10.8 ± 1.4)
WD (°)	227 (189–298)	229 (178–259)	302 (227–33)	229 (229–28)	355 (219–50)	342 (326–351)

To avoid any conceptual ambiguity, we have clarified this terminology in Section 3. We now explicitly frame this period as "relatively stagnant" characterized by substantially reduced regional dispersion.

L262-266: Stagnation and Nitrate explosion (RF3, Dec. 16 AM): This period is characterized by a rapid transition into a relatively stagnation-driven regime...Concurrently, regional meteorological conditions were characterized by decreased wind speed (4.1±2.5 m s-1) and elevated relative humidity (RH) to 72%.

b) Discussing the relative humidity observed at the moment the aerosol is observed. Aerosol have a strong hysteresis effect; therefore, it is important to know the airmass history in order to say if the aerosol is "deliquesce" or "effloresce" at that moment.

We agree with the reviewer that aerosol phase states exhibit hysteresis behavior between the deliquescence and efflorescence relative humidity branches, making the RH history of the air mass a critical consideration.

For the specific perspective of particulate ammonium nitrate, which was the dominant secondary inorganic component during the episode, the temperature-dependent deliquescence relative humidity (DRH) for ammonium nitrate is calculated using the thermodynamic parameterization, given by Seinfeld and Pandis (2006):

$$\ln(DRH) = 723.7/T + 1.6954$$

On Dec. 16 PM, flight-mean RH (74.2%) exceeded the DRH of ammonium nitrate (71.4% at 8.1°C), indicating that ammonium nitrate aerosols were likely present as fully deliquesced aqueous droplets. On Dec. 16 AM, flight-mean RH (71.6%) was marginally below the DRH (72.1% at 7.1°C); however, within the warmer and more humid fraction of the sampled air mass, RH values exceeded DRH, suggesting that deliquescence conditions were at least partially met (Table S2). However, prior transport from drier continental or higher altitudes could introduce phase hysteresis ambiguity. Thus, we revised the relevant sentence as follows.

Table S2. Summary of observed air temperature, ambient relative humidity (RH), and calculated deliquescence relative humidity (DRH) for ammonium nitrate across airborne measurement flights over the Yellow Sea. Values are presented as ranges

from (mean − SD) to (mean + SD). Red text highlights conditions where ambient relative humidity exceeds the DRH (DRH > RH) favoring particle deliquescence.

Flight	Air temperature (°C)	DRH for Ammonium nitrate (%)	RH (%)
Dec. 15 AM	1.70-6.08	75.8-72.8	43.2 ~ 65.0
Dec. 15 PM	3.58-7.66	74.5-71.7	55.0 ~ 74.6
Dec. 16 AM	3.74-10.42	74.4-69.9	61.9 ~ 81.3
Dec. 16 PM	6.55-9.71	72.4-70.4	66.1 ~ 82.3
Dec. 17 AM	1.56-5.12	75.9-73.4	55.1 ~ 75.9
Dec. 17 PM	1.06-5.10	76.3-73.4	50.1 ~ 72.5

L319-325: Within the lower boundary layer, on Dec. 16 AM, flight-mean RH (71.6%) was marginally below deliquescence RH of ammonium nitrate (DRH; 72.1% at 7.1°C; Seinfeld and Pandis, 2006). However, given the substantial variability in RH throughout the flight (53.1–78.9%), a considerable fraction of the sampled air mass experienced RH conditions exceeding the DRH, suggesting that deliquescence conditions were at least partially met. Furthermore, the mutual DRH of internally mixed secondary inorganic aerosol (SIA) is generally lower than that of each constituent pure salt (Seinfeld and Pandis, 2006), making the aerosol population even more susceptible to deliquescence.

c) There is discussion about residual and boundary layer over water at over 1 km. Combination of winter and being over water, it is not intuitive or clear what height the boundary layer, residual layer, and free troposphere would be. Further, would the marine boundary layer be the same boundary layer as what the air had experienced over land, or would there be a decoupling?

We thank the reviewer for this insightful comment. While the marine boundary layer (MBL) is intrinsically shallower than a continental planetary boundary layer (PBL), explicit MBL height data were unavailable over the flight tracks. As an alternative, we evaluated the in situ vertical profiles of rBC mass concentration (M_{rBC}) alongside the ECMWF ERA5 PBL height (PBLH) across all research flights to assess the vertical boundary layer structure and verify the heights of the MBL and residual layer (Figure S3). This approach is based on the fact that BC core is a primary pollutant that neither evaporates nor forms via atmospheric chemical reactions. The PBLH was obtained from the ECMWF reanalysis grid point the observation location.

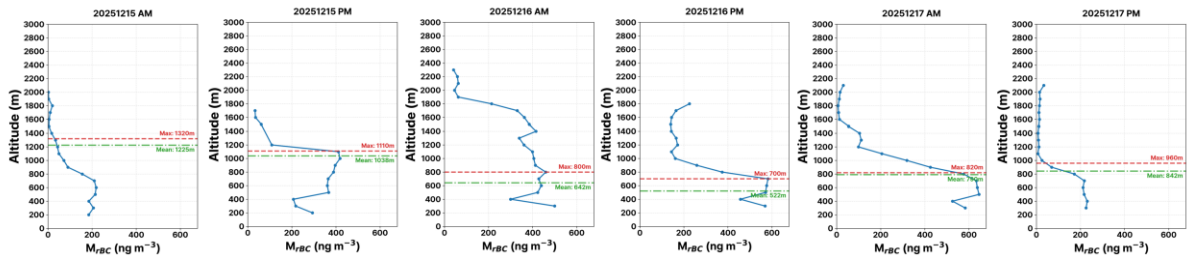

Figure S3. Vertical profiles of M_{rBC} observed during each research flight from 15 to 17 December 2025 over the Yellow Sea. Horizontal dashed lines indicate the estimated planetary boundary layer height (PBLH) obtained from the ECMWF reanalysis at the grid point nearest to the observation location. Red and green dashed lines denote the maximum and mean PBLH, respectively, with annotated values (in m a.s.l.) shown for each flight.

Overall, the observed vertical profiles of M_{rBC} show generally good agreement with the estimated PBLH across the flight campaign. During the 15 Dec. flights (both AM and PM), a sharp decrease in M_{rBC} at approximately 1.0-1.2 km a.s.l. aligns closely with the PBLH. Similarly, for the 16 Dec. PM and 17 Dec. flights, the altitudes at which M_{rBC} decreased rapidly are

broadly consistent with the PBLH, supporting the use of the M_{rBC} vertical structure as an indicator of boundary layer extent. The most notable exception occurred during the 16 Dec. AM flight, where substantial M_{rBC} loadings persisted up to ~1.8 km while the PBLH was estimated near ~600–800 m. This discrepancy suggests that an elevated aerosol layer, likely associated with continental outflow, existed above the shallow marine boundary layer, consistent with a residual layer structure previously reported in the Yellow Sea region (Lee et al., 2019). Given the close correspondence between the altitude of sharp M_{rBC} decreases and the ERA5-derived PBLH across most research flights (Figure S3), the ERA5 PBLH was adopted as the representative boundary layer height for each flight in subsequent analyses. This comparison is added in Sect. S2 in the Supplement.

6. Statements are made without references, either from further analysis or from prior studies. One example is in line 243, saying the air is coming from coal-combustion regions. What leads to this conclusion? Another example is line 275 - 278, where the authors discuss the partitioning of NH3 and HNO3 to aerosol. Where is the NH3 coming from, especially if this is the residual layer? NH3 has a relatively short lifetime, and being in the wintertime, biological sources of NH3, both from agriculture and marine, should be minimal.

1) In line 243, saying the air is coming from coal-combustion regions. What leads to this conclusion?

Recent studies provide comprehensive inventories of operational coal power plants in China (e.g., Cui et al., 2021; Xie et al., 2018), confirming that they are predominantly concentrated across northern, eastern, and northeastern China.

Prior aerosol observations in South Korea during winter also have demonstrated that wind shifts from westerly to northerly frequently correspond to a distinct compositional transition

from nitrate-dominant to sulfate-dominant aerosols. While the observed sulfate enhancement aligns well with these regional patterns, we recognize the reviewer's valid concern regarding over-attribution. Because direct coal-combustion tracers were not measured in flight, attributing the plume exclusively to "coal-combustion regions" remains somewhat speculative. Accordingly, we have removed "coal-combustion" from the text and revised the statement to describe the incoming plume more objectively as a "heavily aged continental airmass from northern upwind regions" to maintain scientific caution.

L288: These extreme values and the decoupled chemical shift demonstrate the direct influx of a heavily aged airmass from northern upwind regions.

2) Another example is line 275 - 278, where the authors discuss the partitioning of NH3 and HNO3 to aerosol. Where is the NH3 coming from, especially if this is the residual layer? NH3 has a relatively short lifetime, and being in the wintertime, biological sources of NH3, both from agriculture and marine, should be minimal.

Although biogenic and agricultural volatilization are typically suppressed during winter, intensive fossil-fuel consumption and residential coal combustion release substantial anthropogenic NH_3 across upwind continental regions (Chen et al., 2022a and b; Lim et al., 2022). Many of both northern China and western Korea operate in an ammonia-rich regime (e.g., Lee et al., 2026).

During offshore transport, continental outflows can potentially be advected within a decoupled residual layer above the boundary layer, which may help mitigate surface dry depositional losses of NH_3 (Lee et al., 2019). Furthermore, relatively low winter temperatures

could thermodynamically disfavor the dissociation of particulate ammonium nitrate, potentially limiting evaporative losses and helping to preserve particle-phase mass during transit.

Previous airborne observations over the Yellow Sea during January–February 2025 (total 16 flights) confirmed substantial ambient NH_3 mixing ratios ranging from 5.23 to 12.41 ppb (reaching peaks of up to 31.12 ppb) under NR-PM_1 loadings of 7.79–25.79 μg m^{-3}; NIER, 2025). As these humidified marine air masses encounter high relative humidity over the Yellow Sea, the favorable low-temperature thermodynamics could promote dynamic gas-particle partitioning, likely facilitating secondary inorganic coatings surrounding BC cores.

L315-322: Therefore, the Dec. 16 AM case likely provided favorable conditions for hygroscopic growth and increased aerosol liquid water (ALW) content, thereby promoting the gas-to-particle partitioning of HNO_3 and NH_3 in aqueous phase and contributing to the observed particulate NO_3^- enhancement. Although NH_3 was not directly utilized in the present study, previous airborne observations over the Yellow Sea during January–February 2025 (total 16 flights) confirmed substantial ambient NH_3 mixing ratios ranging from 5.2 to 12.4 ppbv (reaching peaks of up to 31.1 ppb) under PM1 loadings of 7.79–25.79 μg m^{-3}; NIER, 2025), implying the potential for substantial NH_3 abundance during the study period.

7. Fig. 4 and 5 are uninterpretable. It is now clear how size resolved coating for each component of aerosol measured by AMS is determined, and why some panels are missing data while other panels are not missing data.

The combination of unclear how organics fthick is different from sulfate and the lack of

statistical analysis leads to a disconnect between conclusions and results/discussions.

1) why some panels are missing data while other panels are not missing data.

The missing panels reflect the absence of valid AMS measurements for the corresponding aerosol species during certain flight segments. When AMS-derived concentrations for a given species fell below the detection limit or were otherwise unavailable, the upper/lower 25th percentile conditioning could not be applied, resulting in missing F_{thick} values for those bins. The missing data panels in Figures 4 and 5 are addressed in the revised figure captions, which now explicitly state the reason for data absence.

Figure 4. Size-resolved coating sensitivity of rBC to NR-PM_1 major component, (a) Organic, (b) nitrate, (c) sulfate, and (d) ammonium. Bin 1 (≤140 nm), Bin 2 (140-155 nm), and Bin 3 (≥156 nm) indicate size-dependent rBC group. The blue solid line represents the F_{thick} under the lower 25th percentile mass concentrations of each corresponding aerosol species, while the red solid line denotes the F_{thick} under the upper 25th percentile mass concentrations. The bar graph indicates the difference F_{thick} between the upper and lower 25th percentile F_{thick} values. The analysis was conducted using 1-s data. Missing data indicate unavailable AMS measurements. Statistical significance was evaluated using Kruskal–Wallis *H* tests for each NR-PM_1 component (Supplementary Information S2).

2) The combination of unclear how organics fthick is different from sulfate and the lack of statistical analysis leads to a disconnect between conclusions and results/discussions.

We thank the reviewer for this point. We acknowledge that the differences in F_{thick}

sensitivity among individual chemical components (organics, nitrate, sulfate) are relatively modest and do not individually drive distinct coating behaviors. We have revised the manuscript text accordingly to avoid overstating component-specific differences.

Nevertheless, a physically meaningful pattern emerges when examining the temporal evolution of F_{thick} across rBC core size bins. In Bin 1 (100-139 nm) and Bin 2 (140–155 nm), F_{thick} increased progressively and reached its peak by Dec. 16 AM, whereas in Bin 3 (156-465 nm), the maximum F_{thick} was attained until Dec. 16 PM. This size-dependent temporal offset likely suggests that larger rBC cores require a longer accumulation period to acquire proportionally thick coatings, reflecting size-dependent aging kinetics during the haze episode.

To assess whether these temporal differences in ΔF_{thick} across size bins are statistically meaningful, we performed Kruskal–Wallis H tests. The results confirm statistically significant variation across flight segments for Bin 1 and Bin 2 ($p < 0.001$), with the highest significance in Bin 2 ($p < 0.0001$). Sulfate showed lower statistical robustness ($p > 0.05$) across all bins, consistent with its episodic appearance driven by discrete meteorological events rather than the progressive mass accumulation observed for organic aerosols throughout the campaign.

L415-425: For smaller rBC cores (Bin 1 and Bin 2, 100-155 nm), positive ΔF_{thick} values were distinctly observed up to 0.16 during the early stages of pollution accumulation (from Dec. 15 AM to Dec. 16 AM). The ΔF_{thick} to nitrate and ammonium increase progressively, peaking on Dec. 16 AM in conjunction with the nitrate-rich event under elevated RH (Sect. 3.2), although the differences in ΔF_{thick} responses across individual species were generally modest. ..In contrast, larger rBC cores (Bin 3, 156-465 nm) exhibited a more prolonged response to the evolving pollution event. The coating sensitivity in Bin 3 increased progressively over the first

two days of the campaign, reaching its peak on Dec. 16 PM with ΔF_{thick} values of up to 0.25.

8. The interpretation of the PTR species for sources of organic aerosol is limited.

We agree that the original phrasing overstated the causal role of PTR-measured VOCs in SOA formation. The sentence has been revised to describe the relationship between VOC abundance and rBC aging as an association rather than a direct causal link.

L438: To further characterize the relationship between gas-phase VOC abundance and rBC aging, we examined the coating sensitivity of rBC aerosols to VOC groups.

A) It's unclear how PTR measured "light" VOCs or what "light" VOCs are, as PTR is only sensitive generally to alkenes >C3, aromatics, BVOCs, and OVOCs.

We agree that our previous terminology, "Light-weight C2–C5 VOCs," was ambiguous and did not accurately reflect the measurement capabilities and ion chemistry of PTR-ToF-MS.

In our airborne campaign, target C2–C5 species containing oxygen (such as acetaldehyde and acetone) were assigned to the OVOC category, while isoprene (C5H8) was designated as a biogenic VOC. The primary hydrocarbon signals originally grouped under the "light VOCs" label consisted of high-resolution ToF ions at m/z 41.039 (C3H5+, nominally attributed to propyne/allene isomers) and m/z 43.054 (C3H7+, nominally attributed to propene). Other isobaric ions, such as acetyl cation (C2H3O+ at m/z 43.018), were cleanly resolved and excluded.

However, as the reviewer rightfully notes, these low-molecular-weight carbocations are

susceptible to interferences from dissociative proton transfer (fragmentation) of higher alkanes, alkyl-substituted aromatics, or larger. To maintain the highest scientific rigor and eliminate ambiguity, we have completely removed the "light VOCs" category from both the manuscript text and Figure 5. The revised coating sensitivity analysis in Figure 5 now focuses exclusively on the robustly identified and calibrated VOC classes: aromatic VOCs, oxygenated VOCs (OVOCs), and biogenic VOCs (BVOCs). This revision clarifies the presentation while leaving the primary conclusions of our study intact, as the excluded species previously demonstrated negligible coating sensitivity and lacked discernible trends across all size bins.

L438-443: Volatile organic species were classified into three categories: (1) Aromatic VOCs (including Benzene, toluene, styrene, Ethylbenzene, Xylene, trimethylbenzene), (2) Biogenic VOCs (Isoprene and pinene; BVOCs), and (3) Oxygenated VOCs (OVOCs), which encompassed a broad range of carbonyls and organic acids such as formaldehyde, methanol, acetone, and methyl ethyl ketone.

B) The interpretation of OVOCs being a source of organic aerosol does not reflect the OVOCs being measured, as these OVOCs have too high vapor pressure to ever partition to the aerosol phase.

We thank the reviewer for this important correction. We agree that the low-molecular-weight OVOCs measured in this study including acetone, methanol, formaldehyde, acetaldehyde, and MEK have vapor pressures too high to partition appreciably into the aerosol phase under ambient conditions. The original interpretation overstated their direct role as organic aerosol sources.

We have revised the manuscript accordingly. The positive relationship between OVOC abundance and F_{thick} is now interpreted as a marker of photochemical aging and oxidative processing of the continental air mass, rather than direct condensation of OVOCs onto rBC surfaces. Under such oxidizing conditions, the concurrent formation of lower-volatility products including SVOCs and LVOCs likely contributed to the observed rBC coating growth. This revised interpretation is more physically consistent with the volatility properties of the measured species and has been incorporated into the manuscript text (Sect. 3.3.2).

L450-454: In contrast, aromatic VOCs and OVOCs demonstrated pronounced positive ΔF_{thick} values. The positive relationship between OVOC abundance and ΔF_{thick} is more appropriately interpreted as a marker of photochemical aging and oxidative processing of the air mass. Under such oxidizing conditions, the concurrent formation of lower-volatility products may have contributed to the observed rBC coating growth.

9. Lack of any back trajectories or other airmass history also generally limits the understanding and interpretation of the overall study.

While 72-hour backward trajectory analyses were indeed performed to interpret airmass histories throughout the original analysis, the corresponding trajectory plots were not included in the initial manuscript and have now been incorporated as Figure S2 in the Supplement.

During Dec. 15, northwesterly air masses subsided from higher altitudes (~2,000–3,000 m) across Inner Mongolia and traversed the Beijing–Tianjin–Hebei (BTH) and Northern River Basin regions before arriving over the Yellow Sea within the lower boundary layer (<1,000 m).

This pathway transitioned on Dec. 16 into relatively stagnant, low-level anticyclonic circulation traversing the highly industrialized eastern coastal plains, before shifting abruptly on Dec. 17 to rapid, cold northerly long-range outflow sweeping directly from Northeast China.

L243: **Initial Baseline condition (RF1, Dec. 15 AM):** During the initial period under moderate northwesterly airmass (Figure S2),

L262: **Stagnation and Nitrate explosion (RF3, Dec. 16 AM):** This period is characterized by a rapid transition into a relatively stagnation-driven regime. The airmasses exhibited an anticyclonic curvature, spending extended transport time within the shallow planetary boundary layer before reaching the Yellow Sea (Figure S2). Concurrently, regional meteorological conditions were characterized by decreased wind speed (4.1±2.3 m s^{-1}) and elevated relative humidity (RH) to 74%.

L290: **Clearance (RF6, Dec. 17 PM):** Under strong northerly airmass (Figure S2), sustained strong winds (11 m s^{-1}) eventually swept away the polluted plume in the afternoon.

S1. Aircraft track and airmass backward trajectory analysis

In this study, all six research flights followed highly consistent spatial trajectories over the Yellow Sea. The minor track variations were intentionally designed to capture evolving plume positions as the haze episode progressed, rather than to sample fundamentally different geographic regions.

To investigate air mass origin and transport pathways over the Yellow Sea, 72 h backward trajectories were modeled using the NOAA Hybrid Single-Particle Lagrangian Integrated Trajectory (HYSPLIT) scheme (Draxler and Hess, 1997, 1998; Stein et al., 2015). Calculations were initialized every 10 s along the aircraft track, driven by Global Data Assimilation System (GDAS1) meteorological fields on a 1° × 1° horizontal grid (Figure S2).

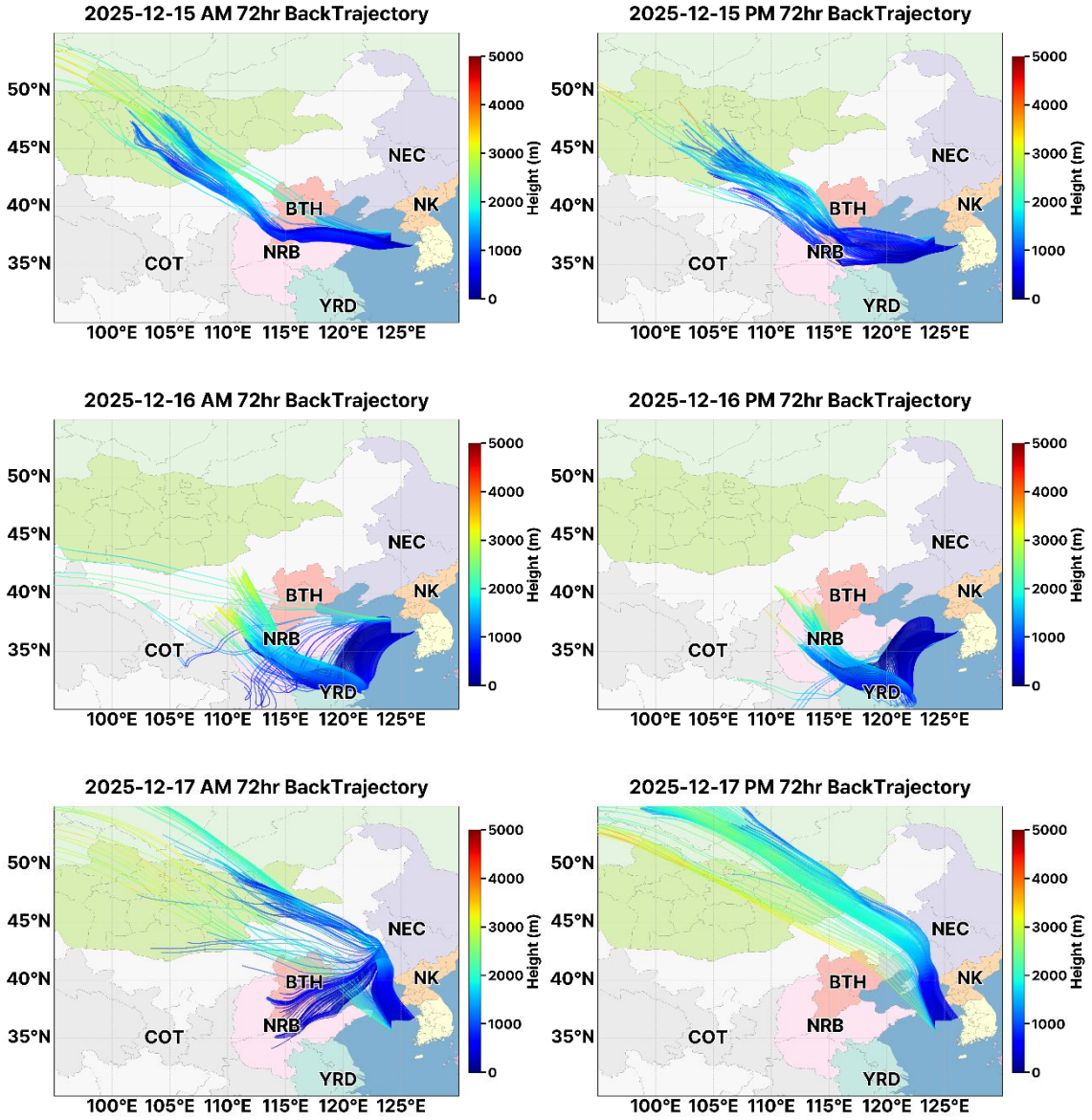

Figure S2. Seventy-two-hour backward airmass trajectories arriving along the flight tracks

over the Yellow Sea for each research flight (15–17 December 2025). The trajectory colors denote the transport altitude above ground level.

10. Both the abstract and conclusion do not fully follow the author guidelines (https://www.atmospheric-chemistry-and-physics.net/policies/guidelines_for_authors.html). This includes the use of abbreviations without defining, comparison and context of the study, caveats, and implications.

We have thoroughly reviewed the ACP Author Guidelines and comprehensively revised both the Abstract and Conclusions sections to ensure full compliance.

Abstract

Atmospheric aging of refractory black carbon (rBC) critically governs its radiative forcing and air quality impacts, yet how discrete chemical transitions sustain continuous physical aging during haze transport remains incompletely understood. Here, we characterize rBC aging behaviors through sequential airborne observations over the Yellow Sea during a winter haze event in 2025. Flight-mean non-refractory submicron particulate matter (NR-PM_1) and rBC concentrations varied within the boundary layer from 3.6 μg m^{-3} to 19.4 μg m^{-3} and 186 ng m^{-3} to 539 ng m^{-3}, respectively, accompanied by a two-phase chemical transition. On 16 December, a nitrate episode (13.4 μg m^{-3} maximum; 9.0 μg m^{-3} flight-mean) coincided with a local peak of thickly-coated rBC fraction, F_{thick} (0.79; 0.64 flight-mean). Sustained high RH above the deliquescence threshold of ammonium nitrate likely promoted nocturnal aqueous-phase processing. A subsequent northerly wind shift on 17 December introduced more aged continental air (sulfate mass fraction 19%, benzene-to-toluene ratio 1.84), elevating flight-

mean F_{thick} to a campaign maximum of 0.70. Despite this air mass shift, the mass fraction of organic aerosol increased progressively from 19% to 28%, tracking the F_{thick} rise. Size-resolved analyses showed smaller rBC cores (100–155 nm) responded rapidly to early aerosol loading, while larger cores (156–465 nm) exhibited delayed but sustained coating growth. These findings reveal that rBC aging was sustained by sequential chemical regime transitions and further differentiated by rBC core size, suggesting that neglecting size-resolved coating dynamics and chemical regime variability may lead to uncertainties in cumulative BC aging estimates in East Asian outflow parameterizations.

Conclusions

Sequential airborne observations over the Yellow Sea during a wintertime haze event revealed that NR-PM_1 chemical composition underwent a pronounced two-phase transition, from a nitrate-dominated regime driven by nocturnal aqueous-phase processing to a long-range transported sulfate-rich plume, rather than simple monotonic accumulation. Coinciding with progressive shifts in photochemical aging indicators (BZ/TOL and MeOH/ACT ratios), F_{thick} rose continuously, reaching a campaign maximum flight-mean of 0.71.

While this chemical regime shift coincided with stepwise F_{thick} increases, the continuous F_{thick} rise was most tightly coupled with the monotonic accumulation of organic aerosol mass fraction (19% to 28%). This is consistent with multi-pathway VOC oxidation providing a steady organic matrix that bridges episodic inorganic transitions and sustains continuous rBC aging. Size-resolved analyses further revealed that smaller rBC cores (100–155 nm) underwent rapid initial encapsulation, while larger cores (156–465 nm) exhibited delayed but sustained coating growth as the air mass matured regionally.

A previous ground-based SP2 study in Seoul during wintertime (Lim et al., 2025)

demonstrated that rBC surfaces actively facilitate secondary aerosol formation when transported plumes arrive at the receptor site under highly oxidized conditions. In contrast to this single-receptor-location measurement, the present study conducted three-dimensional airborne observations across the Yellow Sea, a key transport corridor for East Asian wintertime haze, capturing boundary layer entrainment dynamics alongside spatially-resolved chemical and physical evolution of the aerosol population. Critically, this approach enabled spatially-resolved, size-dependent characterization of rBC aging across a broad outflow pathway, including the possibility of in-situ secondary aerosol growth prior to continental outflow arriving at the downwind receptor region.

These findings are based on a three-day, single-aircraft campaign, and should be interpreted with caution. The short observational period limits broader generalization, and the sampling approach does not allow us to track individual air masses over time or to distinguish primary from secondary organic aerosol contributions to rBC coatings. Nevertheless, these findings suggest that neglecting chemical regime variability and size-dependent coating dynamics in rBC aging parameterizations may introduce substantial uncertainties in cumulative BC aging estimates, with implications for both direct radiative forcing and air quality assessments for the East Asian outflow.

References

Cappa, C. D., Onasch, T. B., Massoli, P., Worsnop, D. R., Bates, T. S., Cross, E. S., Davidovits, P., Hakala, J., Hayden, K. L., Jobson, B. T., Kolesar, K. R., Lack, D. A., Lerner, B. M., Li, S.-M., Mellon, D., Nuaaman, I., Olfert, J. S., Petäjä, T., Quinn, P. K., Song, C., Subramanian, R., Williams, E. J., and Zaveri, R. A.: Radiative absorption enhancements due to the mixing state of atmospheric black carbon, Science, 337, 1078–1081, https://doi.org/10.1126/science.1223447, 2012.

Chen, Z. L., Song, W., Hu, C. C., Liu, X. Y., Walters, W. W., Michalski, G., Zheng, X. D., Li, S. L., Xu, Z. F., Chen, X., Pan, Y. P., Sheng, M. J., Zhang, Y. Y., and Yu, Y. M.: Significant contributions of combustion-related sources to ammonia emissions, Nat. Commun., 13, 7710, https://doi.org/10.1038/s41467-022-35381-4, 2022a.

Chen, Y., Zhang, Q., Cai, X., Zhang, H., Lin, H., Zheng, C., Guo, Z., Hu, S., Chen, L., Tao, S., Liu, M., and Wang, X.: Rapid increase in China's industrial ammonia emissions: Evidence from unit-based mapping, Environ. Sci. Technol., 56, 3375–3385, https://doi.org/10.1021/acs.est.1c08369, 2022b.

Cui, R.Y., Hultman, N., Cui, D. et al. A plant-by-plant strategy for high-ambition coal power phaseout in China. Nat Commun 12, 1468 (2021). https://doi.org/10.1038/s41467-021-21786-0.

Jeong, D., Seco, R., Gu, D., Lee, Y., Nault, B. A., Knote, C. J., McGee, T., Sullivan, J. T., Jimenez, J. L., Campuzano-Jost, P., Blake, D. R., Sanchez, D., Guenther, A. B., Tanner, D., Huey, L. G., Long, R., Anderson, B. E., Hall, S. R., Ullmann, K., Shin, H.-J., Herndon, S. C., Lee, Y. J., Kim, B., Ahn, J., and Kim, S.: Integration of airborne and ground observations of nitryl chloride in the Seoul metropolitan area and the implications on regional oxidation capacity during KORUS-AQ 2016, Atmos. Chem. Phys., 19, 12779–12795, https://doi.org/10.5194/acp-19-

12779-2019, 2019.

Kompalli, S. K., Suresh Babu, S. N., Satheesh, S. K., Krishna Moorthy, K., Das, T., Boopathy, R., Liu, D., Darbyshire, E., Allan, J. D., Brooks, J., Flynn, M. J., and Coe, H.: Seasonal contrast in size distributions and mixing state of black carbon and its association with PM1.0 chemical composition from the eastern coast of India, Atmos. Chem. Phys., 20, 3965–3985, https://doi.org/10.5194/acp-20-3965-2020, 2020.

Lee, H.-J., Jo, H.-Y., Kim, S.-W., Park, M.-S., and Kim, C.-H.: Impacts of atmospheric vertical structures on transboundary aerosol transport from China to South Korea, J. Geophys. Res.-Atmos., 124, 6532–6553, https://doi.org/10.1029/2018JD029751, 2019.

Lee, H., Lee, M., Lim, S., Chang, L.-S., Kim, K., Choi, Y., Park, M.-S., Gil, J., Kim, J.-A., and Yun, C.: PM2.5 nitrate formation during winter haze episodes: insights from Seoul, South Korea, Environ. Sci. Process. Impacts, 28, 998–1014, https://doi.org/10.1039/d5em00589b, 2026.

Lim, S., Lee, M., Laj, P., Kim, S.-W., Ahn, K.-H., Gil, J., Shang, X., Zanatta, M., and Kang, K.-S.: Regional characteristics of fine aerosol mass increase elucidated from long-term observations and KORUS-AQ campaign at a Northeast Asian background site, Elementa Sci. Anthrop., 10, 00020, https://doi.org/10.1525/elementa.2022.00020, 2022a.

Lim, S., Hwang, J., Lee, M., Czimczik, C. I., Xu, X., and Savarino, J.: Robust evidence of 14C, 13C, and 15N analyses indicating fossil fuel sources for total carbon and ammonium in fine aerosols in Seoul megacity, Environ. Sci. Technol., 56, 6894–6904, https://doi.org/10.1021/acs.est.1c03903, 2022b.

Lim, S., Bae, M.-S., Jang, J., Dwivedi, A. K., Gil, J., Kim, J., Lee, M., Oh, S.-H., Shin, S.-A., and Chang, L.-S.: Exploring fine-aerosol episodes in urban Seoul during the cold season of the 2021 SIJAQ campaign: measurement evidences of heterogeneous reactions on black

carbon particles, Atmos. Environ., 342, 120926, https://doi.org/10.1016/j.atmosenv.2024.120926, 2025.

Liu, D., Whitehead, J., Alfarra, M. R., Reyes-Villegas, E., Spracklen, D. V., Reddington, C. L., Kong, S., Williams, P. I., Ting, Y.-C., Haslett, S., Taylor, J. W., Flynn, M. J., Morgan, W. T., McFiggans, G., Coe, H., and Allan, J. D.: Black-carbon absorption enhancement in the atmosphere benefited by coatings, Nat. Geosci., 10, 184–188, https://doi.org/10.1038/ngeo2901, 2017.

Liu, D., Joshi, R., Wang, J., Yu, C., Allan, J. D., Coe, H., Flynn, M. J., Xie, C., Lee, J., Squires, F., Kotthaus, S., Grimmond, S., Ge, X., Sun, Y., and Fu, P.: Contrasting physical properties of black carbon in urban Beijing between winter and summer, Atmos. Chem. Phys., 19, 6749–6769, https://doi.org/10.5194/acp-19-6749-2019, 2019.

NIER: Aircraft observation for advanced multi-platform observation (I), National Institute of Environmental Research (NIER), Incheon, Republic of Korea, Final Report, 566 pp., 2025.

Peng, J., Hu, M., Guo, S., Du, Z., Zheng, J., Shang, D., Levy Zamora, M., Zeng, L., Shao, M., Wu, Y.-S., Zheng, J., Wang, Y., Glen, C. R., Collins, D. R., Molina, M. J., and Zhang, R.: Markedly enhanced absorption and direct radiative forcing of black carbon under severe haze conditions, P. Natl. Acad. Sci. USA, 113, 4266–4271, https://doi.org/10.1073/pnas.1602310113, 2016.

Riemer, N., West, M., Zaveri, R. A., and Posfai, M.: Estimating black carbon aging time-scales with a particle-resolved aerosol model, J. Geophys. Res.-Atmos., 115, D08209, https://doi.org/10.1029/2009JD012628, 2010.

Seinfeld, J. H. and Pandis, S. N.: Atmospheric chemistry and physics, 2nd edn., John Wiley & Sons, Hoboken, NJ, 2006.

Teng, X., Du, M., Song, C., Dai, Y., Lal Chandani, V., Beddows, D. C. S., Dall'Osto, M., Baumgardner, D., Harrison, R. M., Brean, J., Yang, M., Zhang, Y., Li, W., and Shi, Z.: Greenland emissions contribute to black carbon aerosols in the Arctic marine boundary layer, Environ. Sci. Technol., https://doi.org/10.1021/acs.est.6c03343, 2026.

Xie L, Huang Y, Qin P. Spatial distribution of coal-fired power plants in China. Environment and Development Economics. 2018;23(4):495-515. doi:10.1017/S1355770X18000098.

Zanatta, M., Laj, P., Gysel, M., Baltensperger, U., Vratolis, S., Eleftheriadis, K., Kondo, Y., Dubuisson, P., Winiger, P., Schultz, M. G., and Schmale, J.: Sizing and optical properties of black carbon particles in the European Arctic, Atmos. Chem. Phys., 18, 7815–7837, https://doi.org/10.5194/acp-18-7815-2018, 2018.